

Estimating Geographical PV Potential Using LiDAR Data for Buildings in Downtown San Francisco

Ziqi Li, Zidong Zhang and Keith Davey

Department of Geography and Environment Management, University of Waterloo

Abstract

Sustainable solar energy is of the interest for the city of San Francisco to meet their renewable energy initiative. Buildings in the downtown area are expected to have great photovoltaic (PV) potential for future solar panel installation. This study presents a comprehensive method for estimating geographical PV potential using remote sensed LiDAR data for buildings in downtown San Francisco. LiDAR derived DSMs and DTMs were able to generate high quality building footprints using the object-oriented classification method. The GRASS built-in solar irradiation model (*r.sun*) was used to simulate and compute PV yields. Monthly and yearly maps, as well as an exquisite 3D city building model, were created to visualize the variability of solar irradiation across the study area. Results showed that monthly sum of solar irradiation followed a one-year cycle with the peak in July and troughs in January and December. The mean yearly sum of solar irradiation for the buildings in the study area was estimated to be 1675 kWh/m². A multiple regression model was used to test the significance of building height, roof area and roof complexity against PV potential. Roof complexity was found to be the dominant determinant. Uncertainties of the research are mainly from the inherent *r.sun* limitations, boundary problems, and the LiDAR data accuracy in terms of both building footprint extraction and 3D modeling. Future work can focus on a more automated process and segment rooftops of buildings to achieve more accurate estimation of PV potential. The outcome of this research can assist decision makers in San Francisco to visualize building PV potential, and further select ideal places to install PV systems. The methodology presented and tested in this research can also be generalized to other cities in order to meet contemporary society's need for renewable energy.

1 Introduction

Sustainability has been a major topic of interest for the City of San Francisco, which has set an ambitious initiative to meet their energy demand with 100% renewable energy sources by the year 2020 (City and County of San Francisco 2006). Sources of renewable energy such as solar, wind, hydro, geothermal, and biofuels have been extensively evaluated and policies and programs put in place to address the city's energy goals (Adelaja et al. 2010). Solar energy in particular offers the possibility of replacing fossil fuels in the near future by offering a sustainable way to generate electricity for contemporary society's need (Pearce 2002; Liu and Wu 2010). Moreover, photovoltaic (PV) technology to convert solar energy directly into electricity has been proved to be technologically robust, environmentally friendly, geographically distributable, and potentially sustainable (Nguyen and Pearce 2010). Those characteristics of solar energy attract vast cooperation and technology investment in photovoltaic (PV), which assists in the discovery of sites with high geographic potential that contribute to solar cell efficiency

Address for correspondence: Ziqi Li, Department of Geography and Environment Management, University of Waterloo, Waterloo, Ontario N2L 3G1, Canada. E-mail: liziqi1992@gmail.com

Acknowledgements: The authors wish to acknowledge Department of Geography and Environment Management, University of Waterloo for providing pre-processed LiDAR DSM and DTM. Also, we gratefully appreciate Prof. R. Kelly from University of Waterloo for his valuable guidance on this project. Special thanks to Mike Lackner and Grant Gunn for their help in the lab.
Authors contributed equally

(Nguyen et al. 2012). By April 2013, the City of San Francisco reports that they own 3,747 installed PV systems, which would generate approximately 31,113 MWh electricity and reduce 6,282 metric tons of CO₂ per year (City and County of San Francisco 2014).

1.1 Context

1.1.1 Solar energy potential modeling

Sophisticated solar energy potential modeling techniques significantly contribute to the development of photovoltaics. There are three general approaches to compute solar radiation potential: (1) field-based; (2) satellite-based; and (3) fusion of field- and satellite-based (Angelis-Dimakis et al. 2011). The third approach is the most frequently selected method using data from both meteorological stations and satellites (Angelis-Dimakis et al. 2011). Satellite data are used to compensate for the limited data available from meteorological stations. There are several solar radiation databases (e.g. European Solar Radiation Atlas (ESRA), NASA Surface meteorology and Solar Energy, and Meteonorm) that contain solar radiation data for the global and continental scales but not for the regional scale (Šúri and Hofierka 2004; Angelis-Dimakis et al. 2011). For the regional studies, there is a trend towards integrating geographical information systems (GIS) with solar radiation models to provide accurate, fast, cost-saving simulations of radiation considering terrain effects and atmospheric attenuation (Šúri and Hofierka 2004). There are several GIS-based solar radiation models created during the last decade: SolarFlux with ArcInfo, AML script with Genasys GIS, Solei with IDRISI, Solar Analyst with ArcGIS, and *r.sun* with GRASS (Geographical Resources Analysis Support System) (Herrick et al. 1993; Dubayah and Rich 1995; Mészáros et al. 1998; Šúri and Hofierka 2004; Hofierka and Kaňuk 2009). Those solar radiation models take in solar, geographic and atmospheric parameters and use GIS or remote sensing as the data sources. Solar parameters are constant, and atmospheric parameters can be obtained from meteorological station records. For the geographical parameters, researchers have proposed using techniques utilizing remote sensed data to acquire terrain information for estimating solar energy potential (Jochum et al. 2009; Carneiro et al. 2009; Kassner et al. 2008). During the last decade, there was a trend to integrate remote sensing technology as input with solar irradiation models because of the high quality, availability and scalability of remotely sensed data (Nguyen and Pearce 2012). The solar models can be used in practice to make cities more sustainable, since it is energy-efficient to integrate solar panels on the top of city buildings (Boyle 2004).

1.1.2 Building footprint generation

With the rapid development of urbanization, a large number of buildings have been built or rebuilt in the last decades. Additionally, the advances in urban planning and design, along with technical support such as new energy-saving construction materials and precise 3D modeling, has altogether resulted in a dynamic city. This increases the difficulty of acquiring a real-time city building footprint map with high accuracy, which is valuable in urban planning, transportation, and other commercial decision-making.

Most current building footprints come from manually digitizing from high-resolution satellite imagery or in-field surveying, which is both time-consuming and expensive (Shackelford et al. 2004). A major concern with this kind of building footprint is the data quality, since the manual drawing process is subjective and varies greatly from person to person. So there is no standard and effective ways to ensure the accuracy and completeness of data. In addition, this approach creates information islands (Li et al. 2013) where the footprint of a city is measured

and stored in different places which cannot communicate and collaborate virtually. The unscalable method implies that there is no way of automating the process because the task load is a linear function of the size of the target areas.

Very high resolution, meter and sub-meter level satellite imagery such as QuickBird, WorldView and IKONOS has been developed rapidly in the last decades, creating widespread interest object-oriented image analysis. The object-based image classification looks for both spectral and spatial features of image objects. Compared with pixel-based classification, this object-oriented approach effectively removes “salt and pepper” noise. There are now also non-optical data successfully used for object-based building extraction, such as high resolution LiDAR (Light Detection and Ranging) data (Rottensteiner and Briese 2002) and LiDAR derivatives including DEMs (Digital Elevation Models) and DSMs (Digital Surface Models).

1.1.3 3D modeling

Interest in constructing 3D models has grown rapidly over the last decade, and has become a valuable tool for decision makers to better visualize complex datasets and large geographic areas in order to make more informed decisions. LiDAR data is the most popular and commonly used dataset for building 3D models, utilizing point elevation data as well as derived DSMs and DTMs (Digital Terrain Models) to classify building objects and construct polygon objects with the capability of discerning features such as roof structure and type (Elaksher and Bethel 2002; Forlani et al. 2006; Tse et al. 2008; Zhou and Neumann 2008). Aerial photography presents another dataset capable of modeling building structures using the geometric properties of the camera position with respect to the perceived buildings (Fischer et al. 1998; Moons et al. 1998). Hybrid approaches to 3D modeling also exist, utilizing a wealth of different remotely sensed data which enhance the previous models by utilizing spectral data, as well as existing ground plans and map data to further distinguish discrete objects with more precision and accuracy (Syed et al. 2005; Haala and Brenner 1999). A review of the existing literature on the subject of constructing 3D models of urban environments revealed a number of important themes. The first was that the feature being modeled is of utmost importance in considering what type of data to utilize when developing a 3D model. The second was the resources available for the construction of the 3D model, including, but not limited to, time, money and computational power (Liang et al. 2014). The third was data quality, as some construction techniques have more stringent requirements data quality than others.

1.2 Research Question and Objectives

The research was built upon the work of the San Francisco Solar Map project (<http://sfenergymap.org>) to fill the knowledge-gap in current research, which does not try to model photovoltaic potential for individual buildings, but sets the focus at a larger scale. In San Francisco there is no existing study that analyses the PV potential at the building object level, and no existing 3D PV potential models. In this project, the research question was “what is the geographical photovoltaic potential for buildings in downtown San Francisco?”

There were three objectives in asking the research question:

1. To implement an object-oriented classification on LiDAR derivatives to extract building footprints;
2. To compute geographical PV potential of extracted buildings and
3. To visualize the results of the PV potential in a 3D model.

2 Methodology

2.1 Study Area, Data and Workflow

The study area (Figure 1) was a 1 km region in the northeastern part of the City of San Francisco. The region was chosen due to its unique characteristics which has strong urban presence, being dominated by high density tall buildings, and being used primarily for commercial business. The City was first settled in 1776, and incorporated in 1850 (City and County of San Francisco 2006). As of 2012, the population of the area is estimated to be 825, 000 inhabitants (US Census Bureau 2012). The City is situated on a natural harbor, serving as a gateway for international imports and exports to and from the US. As part of Silicon Valley, alongside Cupertino, Palo Alto, San Jose, and Mountain View, San Francisco has seen a population boom over the past few decades, growing approximately 2.6% of its population in the years from 2010 to 2012 (US Census Bureau 2012). This population boom has seen a rapid growth and investment into core infrastructure, and the construction of new buildings to support the demand for high tech startups (City and County of San Francisco 2006). The rapid growth in the area has seen an added pressure on the City to implement their 100% renewable energy agenda.

The raw data was provided by the University of Waterloo and consisted of a set of LiDAR data captured in June 2010, with derived DEMs and DSMs, at a 0.5 m resolution. The projected coordinate system is EPSG: 26910 (NAD83 / UTM zone 10N). The LiDAR data is

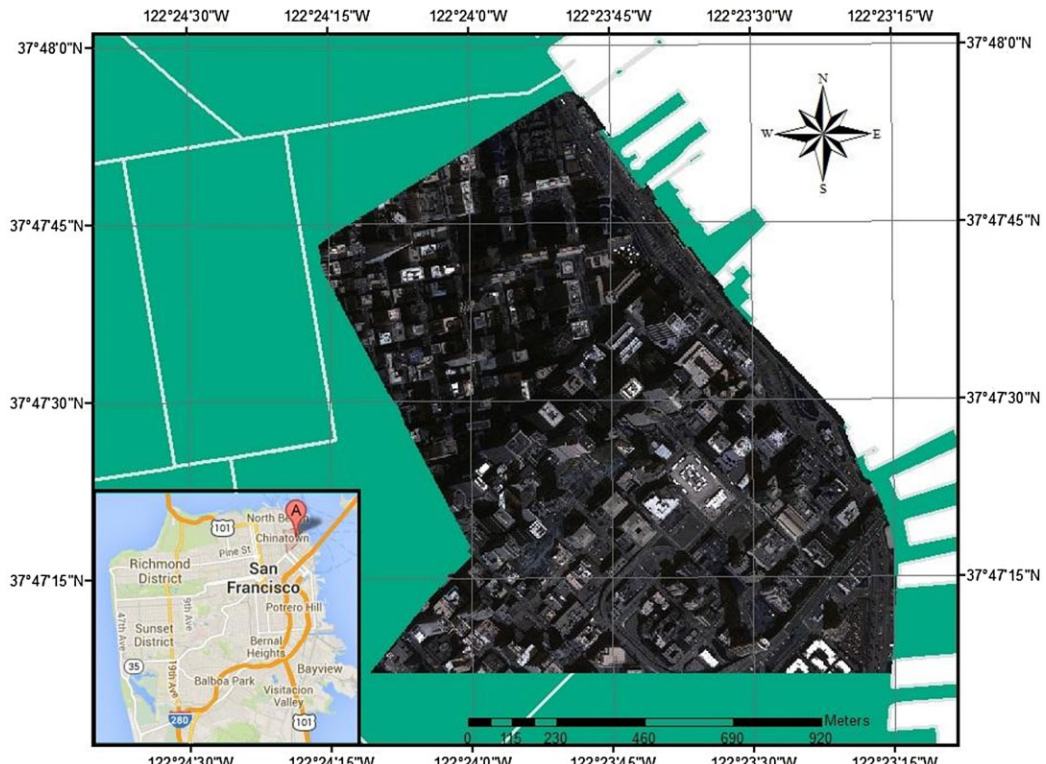


Figure 1 Study area map

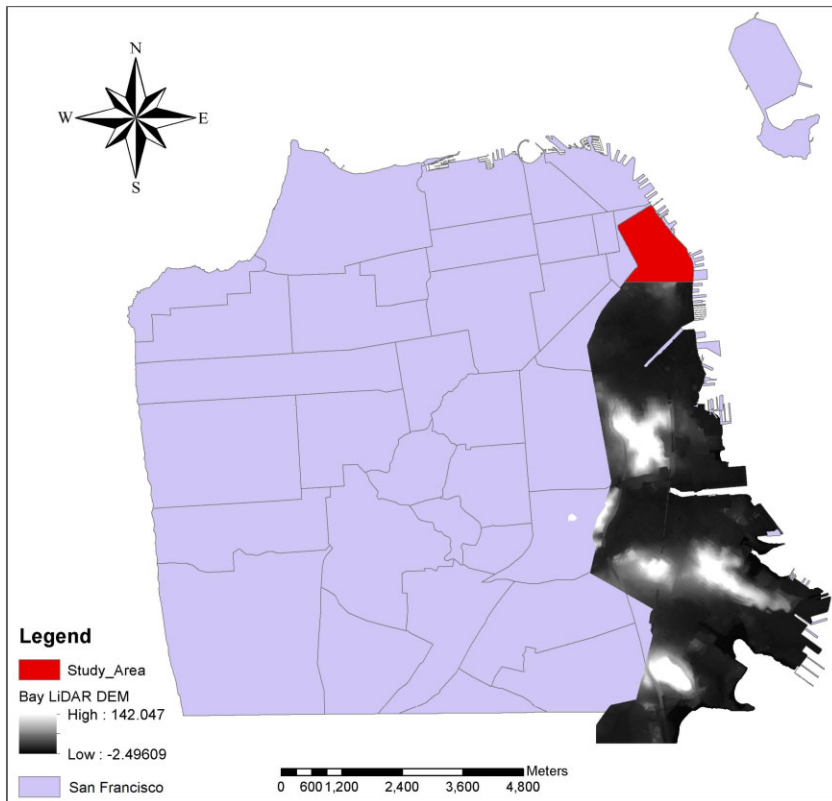


Figure 2 LiDAR DEM scale

available for the east bay region of San Francisco. The DEM data scale, which is a subscale of the DSM, is shown in Figure 2.

In response to the three objectives, the project was divided into three main components as represented in Figure 3. The very first process was to extract high-quality building footprints to facilitate later steps. Then, a PV potential analysis was performed on the buildings. The last component was to construct 3D model of the City and visualize the results of the PV potential analysis. There were also other pre-processing steps to project all the data sets to WGS 84 / UTM zone 10N and clip the origin LiDAR data to the study area size using ArcGIS 10.2.

2.2 Object-Oriented Building Extraction

2.2.1 Image segmentation

In object-based classification methods, the very first step is to perform image segmentation at the pixel level. In the process, pixels are grouped to form objects and object pieces to aid in later image analysis and land cover extraction. There are several developed segmentation software packages widely used in this field such as eCognition and SPRING. In 2004, Meinel and Neubert (2004) published a paper evaluating the segmentation quality of seven major software and found that eCognition had the highest overall quality. Thus in this project, eCognition was chosen to perform the image segmentation, using the multiresolution

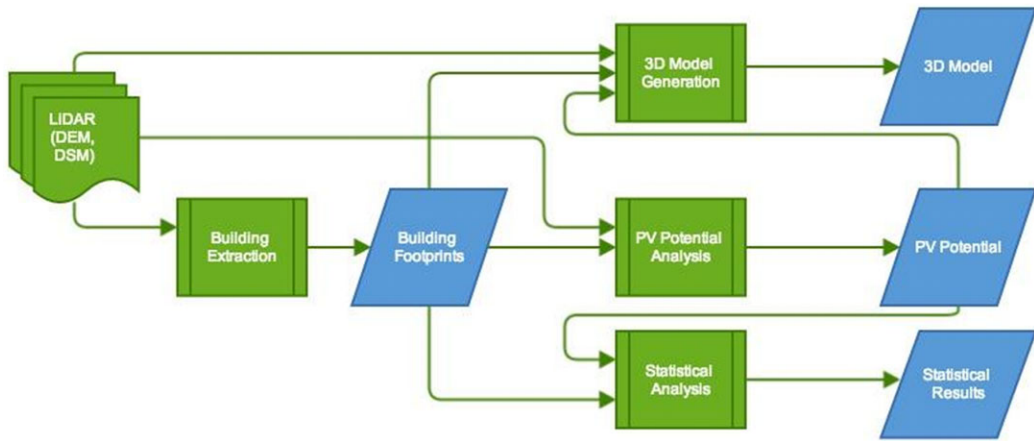


Figure 3 Workflow

segmentation algorithm (Baatz and Schäpe 2000), a region growing approach which has been widely adopted (Liu et al. 2006). The algorithm needs three input parameters: (1) shape, which is the weight ($0 \leq \text{shape} \leq 1$, color = 1-shape) for shape characteristics versus color characteristics; (2) compactness, which is the weight ($0 \leq \text{compactness} \leq 1$, smoothness = 1-compactness) for the compactness criterion versus the smoothness criterion; and (3) scale parameter, which is a non-unit value that determines the maximum allowed heterogeneity change resulting from image merging, so a higher scale value will indirectly result in larger objects.

Previous studies (Sohn and Dowman 2007; Rottensteiner and Briese 2002, 2003) have used LiDAR data to extract buildings successfully. Examining the DEM and DSM images created by LAStools, it was found that building height and roof shape were the most predominant factors that can distinguish buildings from other objects. So the building height image was used for building extraction. The building height image created was exported to Geo-TIFF format. Since the exported image should be a rectangular shape, there were some no-value pixels and these were set to 255. The image was calculated in ArcGIS as (Figure 4):

$$\text{Building Height} = \text{DSM} - \text{DEM} \quad (1)$$

In the process, different input parameter sets were experimented with and the results were compared carefully to produce a high-quality segmentation product. The optimal combination of input parameters was given so that when the scale parameter was set to 50, shape was set to 0.5, and compactness was set to 0.5.

2.2.2 Rule-based building extraction

In this phase, several features (Table 1) of building objects were used to extract buildings. A decision tree (Figure 5) was established to filter out non-building pieces, select building objects, and merge building pieces. Some features were used more than once and some additional object reshaping steps were taken, such as aggregating objects into one single bigger object via merging, which is an effective method of minimizing the “salt and pepper” noise. The first rule was to filter out segments outside the study area, which was set to 255 in the previous step.

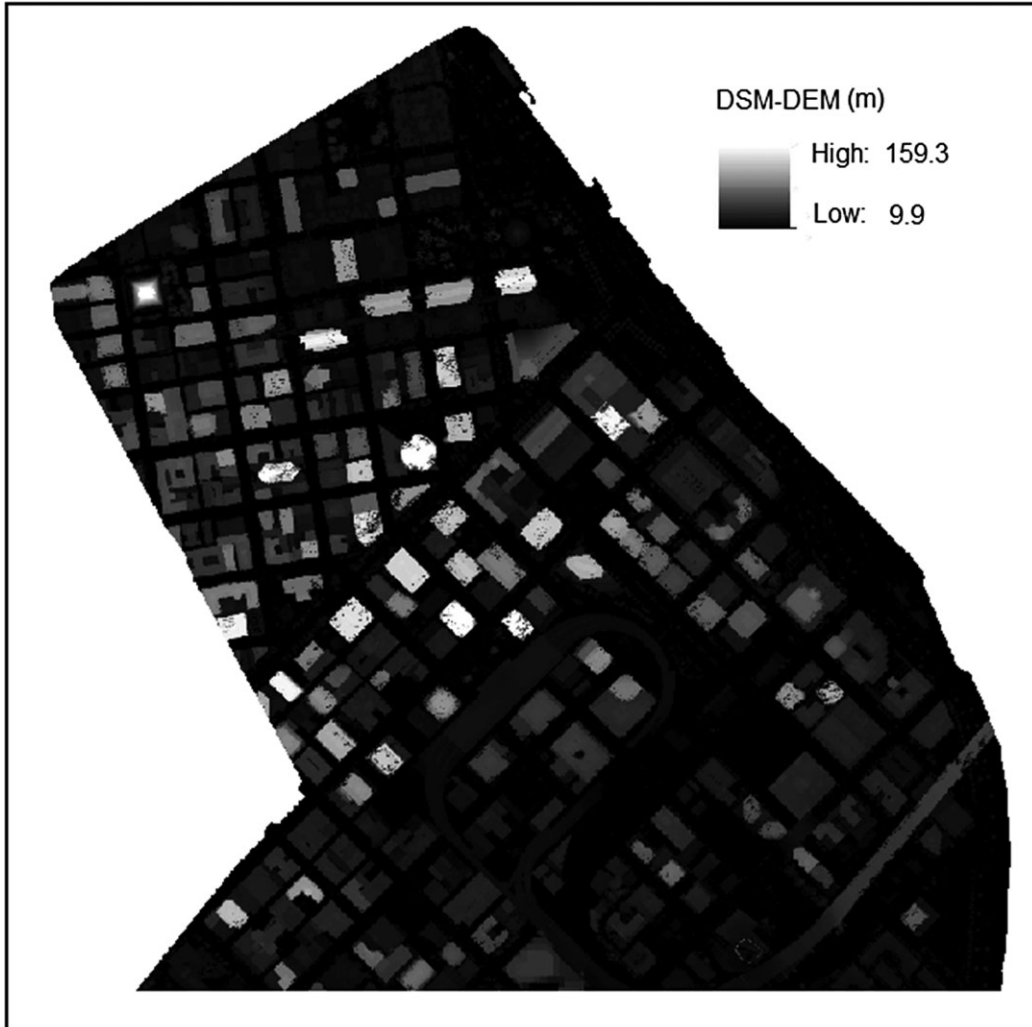


Figure 4 Image of building height (difference of DEM and DSM)

Table 1 Features for building extraction

Feature Name	Description
Building Height	The elevation thematic layer will be produced from DEM and DSM data. Objects above a certain elevation level will be classified to building type.
Rectangular Fit	Buildings are more likely to have a rectangular shape than other land cover types
Length / Width	Can be used to filter out roads, streets, etc.
Area	Area of the building roof. Can be used to filter out very small segments.

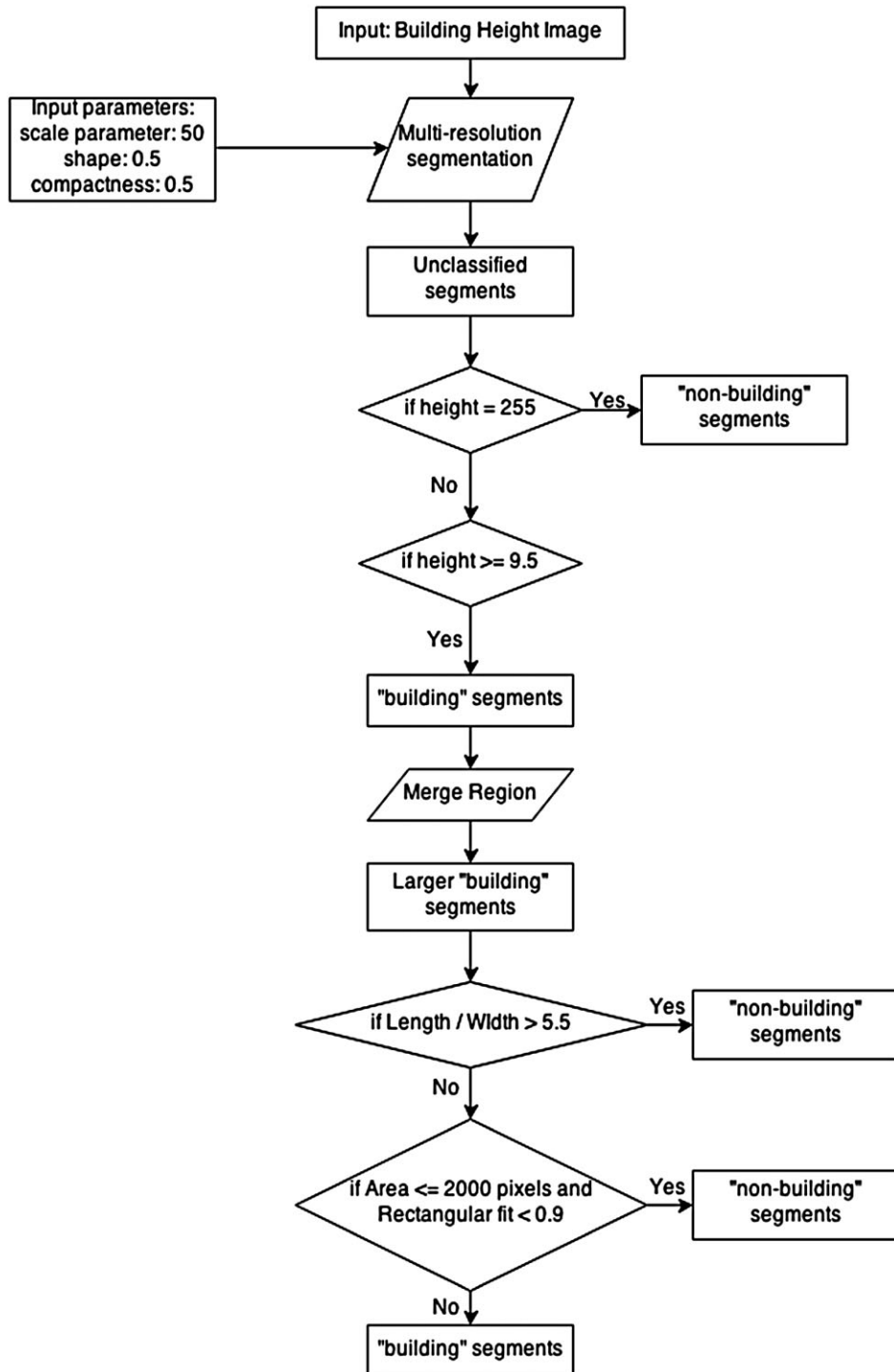
**Figure 5** Decision tree



Figure 6 Misclassification (viaduct)

These segments were classified to the “non-building” group. Next, the building height value was used to classify segments to the “building” group. Several experiments were conducted and 9.5 m was the chosen threshold to minimize the number of incorrectly classified segments and maximize the number of actual building pieces. Segments with a height equal to or above 9.5 m were treated as buildings. Then the “merge region” step was taken to merge adjacent building segments to one single object. This essential step eliminated very fine segments by merging them with their neighbors. By examining the result after this step, an obvious misclassification was seen in the right-hand bottom corner of the input image. Shown in Figure 6, this area has complex information, where part of a building roof is blocked by the viaduct above it. Therefore a following step was taken to delete this incorrect classification, utilizing the feature “Length / Width”, since the viaduct has a very high “length / width” value. There were also other misclassifications such as trees and street lights. These incorrectly classified objects have a smaller area and less rectangular fit value than actual buildings. So another filter was added to the building group. Figure 7 showed the final result. The “building” objects were exported to shapefile format.

2.3 Photovoltaic Potential Simulation

2.3.1 Model description

PV potential analysis was performed based on the extracted building footprints from the LiDAR data. PV converts solar radiation into electricity. In this study, the “geographical” PV potential was of the interest, which indicates the total amount of solar radiation that can be received on buildings. The term solar irradiation is solar radiation received for a given time per unit which is used as the indicator of geographical PV potential in this study. The solar irradiation model (*r.sun*) integrated in the Geographic Resource Analysis Support System (GRASS) was applied to simulate the interaction between the Sun and the Earth and to quantify the geographical PV



Figure 7 Intermediate result of buildings (yellow) and non-building objects (red)

potential of a group of solar, geographic, and atmospheric parameters (Nguyen and Pearce 2012). The *r.sun* model uses algorithms in the latest research conducted for the European Solar Radiation Atlas (ESRA) project (Scharmer and Greif 2000; Rigollier et al. 2000). The integration of *r.sun* within GRASS can reduce the computational complexity. Another reason to choose *r.sun* is that the model can incorporate shadowing effects which are considered significant in downtown areas with tall buildings and high building density.

In this study, the inputs of the *r.sun* model are building-clipped surface elevation, slope and aspect of the terrain, as well as monthly Linke Turbidity Factor (T_L) which denotes the transparency of the atmosphere. Terrain information was extracted from the existing DSM. The T_L data were retrieved from the worldwide database of the Linke Turbidity Factor provided by the Solar Radiation Database for Environment SoDa Service website. The *r.sun* model can output direct (beam), diffuse and reflected solar irradiation maps, respectively. In this study, the total solar irradiation, which combined all three sources, is of interest. Therefore, the outcome of the *r.sun* model was a series of daily total horizontal solar irradiation raster maps, which were then aggregated on both a monthly and yearly basis. In this article, to simplify, the word “solar irradiation” refers to total horizontal solar irradiation. The resolution of the output raster maps is the same as that of the input DSM, which is 0.5m, and all data are in floating point format.

2.3.2 Terrain inputs

All terrain parameters were extracted from the DSM. The DSM was clipped by extracted building footprints using the *r.mask* tool to get the clipped DSM map so that all other features on the

ground except for buildings were filtered. Then, the clipped DSM as the input was used to generate slope and aspect maps using the `r.slope.aspect` tool. To be more specific, values in the slope map are the angles of the inclination from the horizontal plane. Values in the aspect map shows the directions that slopes are facing, which means 90 is North, 180 is West, 270 is South, and 360 is East.

2.3.3 Linke Turbidity factor

The Linke Turbidity factor (T_L , normalized at an air mass = 2) is a surrogate to estimate the atmospheric absorption and scattering of the solar radiation under clear-sky conditions (Ineichen and Perez 2002). The factor indicates the optical thickness of the atmosphere resulting from the absorption by the water vapor and the absorption and scattering by the aerosol particles relative to a dry and clean atmosphere. More generalized, the T_L describes the turbidity of the atmosphere and therefore the attenuation of the solar radiation (Kasten 1996). The T_L value has a positive correlation with the attenuation, which means the larger the T_L , the more turbidity in the atmosphere, and the larger the attenuation of the solar radiation. If the T_L equals 1, it is assumed that the sky is theoretically dry and clean. The T_L has a typical value around 3 globally (Kasten 1996).

In the context of San Francisco (Table 2), the Linke Turbidity Factor is around 3.3 yearly. Summertime has higher atmospheric turbidity than wintertime. The highest value is in the summer (3.6 for July), and lowest value is in the winter (3.0 for December). All T_L values were retrieved from the worldwide database of the Linke Turbidity Factor through the SoDa Web Service. Detailed information of the algorithms to construct the database can be found on the SoDa Website (<http://www.soda-is.com/publications/index.html#link>).

2.3.4 Optional inputs and settings

Ground albedo and a real-sky index are two optional inputs in `r.sun` model. In this study, the albedo value was set to the constant default which is 0.2. The reflected irradiation is sensitive

Table 2 Monthly Linke Turbidity Factor near San Francisco

Month	Linke Turbidity Factor (T_L)
January	3.3
February	3.3
March	3.2
April	3.2
May	3.5
June	3.5
July	3.6
August	3.5
September	3.4
October	3.2
November	3.1
December	3.0
Yearly	3.3

to the albedo value. However, the contribution of ground reflected radiation is negligible when albedo is taken as 0.2 and only horizontal radiation is considered (Hofierka and Šúri 2002; Šúri et al. 2005). Also, the city of San Francisco is free of snow presence, which does not meet the situation described by Duffie and Beckman (1991) that errors can be substantial when using a constant 0.2 and if ground reflectance is between 0.6 and 0.7 as is typical of snow. What is more, previous work has incorporated an albedo map in Kingston, ON, Canada (Nguyen and Pearce 2010). The results indicated that the beam and diffuse irradiation are in the order of kWh while ground reflection is in the order of Wh only. So a constant value of 0.2 for albedo is sufficient in this study. The real-sky index, which is denoted as the fraction of the clear-sky radiations reduced by atmospheric factors, was excluded because solar radiation under clear-sky condition was the focus in this research.

The *r.sun* model has two modes. The output of mode 1 is to calculate the solar irradiance for a specified local time, and the output of mode 2 is to calculate the sum of solar irradiation within a specified day. In this study, mode 2 was selected to produce a set of daily, monthly and yearly solar irradiation maps. A time-step of 0.5 h was selected when computing all-day radiation sums. The “Incorporate the shadowing effect of terrain” option was checked because in Downtown San Francisco, skyscrapers are expected to have significant shadowing effects on relatively shorter neighboring buildings.

2.3.5 Transformation from pixel- to building-based

The outputs of the *r.sun* model are raster maps with a 0.5m spatial resolution. Raster maps were then imported into ArcGIS 10.2 Desktop. The Zonal Statistics tool was used to aggregate pixels into buildings based on building boundaries. The zone data was the extracted building footprints, and values were from solar irradiation rasters with the footprint ID as the zone field. The statistic option was set to be MEAN so that the average of solar irradiation values of pixels, within a building boundary, was assigned to that building. The MEAN option is selected instead of SUM because the unit of solar irradiation is kWh/m² which is a solar flux density indicator. Averaged values represent building's overall PV potential, excluding the influence of area of building footprints. Zoned solar irradiation values were then matched with the building footprints shapefile based on building footprint ID. The joined shapefile was stored and used for subsequent analysis and 3D modeling.

2.3.6 Processing procedures

All procedures were automated and completed in GRASS 7.0 using predesigned shellscript. Steps are visualized in Figure 8 and summarized as follows:

1. The DSM of the entire study area was clipped by extracted building footprints using *r.mask* tool to get the clipped DSM map.
2. The clipped DSM as the input was used to generate slope and aspect maps using the *r.slope.aspect* tool.
3. The clipped DSM, slope map, aspect map and the monthly Linke Turbidity Factor were input into the *r.sun* model to generate daily total irradiation maps. The “Incorporate the shadowing effect of terrain” option was checked. This process was iterated 365 times, with different T_L for each month.
4. Daily irradiation maps were then aggregated to monthly maps from January to December using the *r.series* tool with the “method: sum” option.

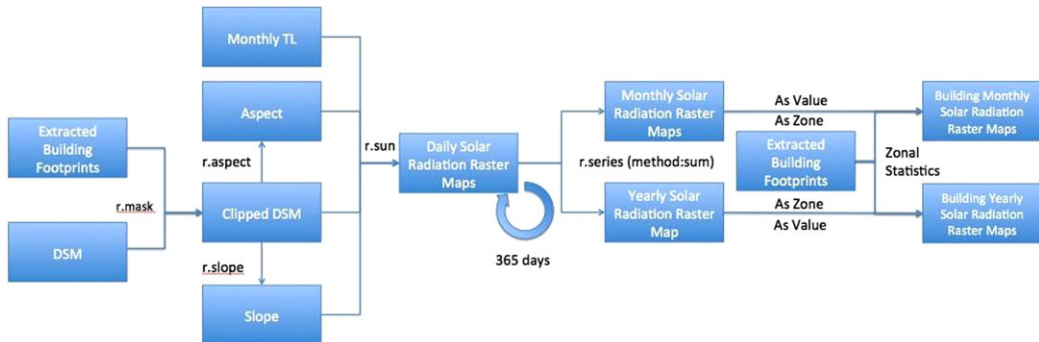


Figure 8 Processing flow of solar irradiation calculation

5. The same procedure as (4) was used to aggregate monthly solar irradiation maps into one yearly solar irradiation map.
6. Solar irradiation rasters were zoned based on extracted building footprints using the Zonal Statistic tool in ArcGIS 10.2.
7. Monthly and yearly solar irradiation maps were created.

2.4 3D Modeling

The construction of a 3-dimensional model was an important visualization step to our methodology to better communicate our findings to the decision-makers of the City of San Francisco for their consideration of the placement of solar cells on building rooftops. There are a number of intermediate steps and datasets that are common to the three main objectives of our research statement, but the addition of refinements to optimize the 3D model are required. The first piece of data that acted as a prerequisite to building the 3D model was a shapefile representation of the building footprints extracted in the classification stage, with the associated PV potential values. The second piece of data required was a raster elevation representation of the study area in the form of both a DTM and a DSM. Utilizing this data, a model was developed using the Esri's ArcGIS ArcGlobe platform, part of the ArcGIS for Desktop 3D mapping platform for the Microsoft Windows Operating system (<http://www.esri.com/software/arcgis/arcgis-for-desktop>). Figure 9 represents the process flow of the 3D modeling objective.

2.4.1 Building footprint height tagging

The building footprints extracted in the previous steps of our research form the basis of the 3D visualization of the Downtown region of San Francisco. Using this footprint shapefile, the first step to preparing data for 3D visualization within ArcGIS's ArcGlobe is to attribute each building footprint with its associated building height. To attribute building footprints with their associated building heights, the zonal statistics contained within ArcGlobe were utilized. Running the Zonal Statistics to Table tool within the zonal statistics toolset required a number of input files and parameters to run. The first file required to run the tool was the zone dataset of the building footprint, provided in the form of a shapefile with the footprint ID as the corresponding field to uniquely identify each building and match it to the original feature. The second input dataset required was a raster containing the height for each pixel. The input dataset used for this step was the previously defined raster of building height (Equation 1).

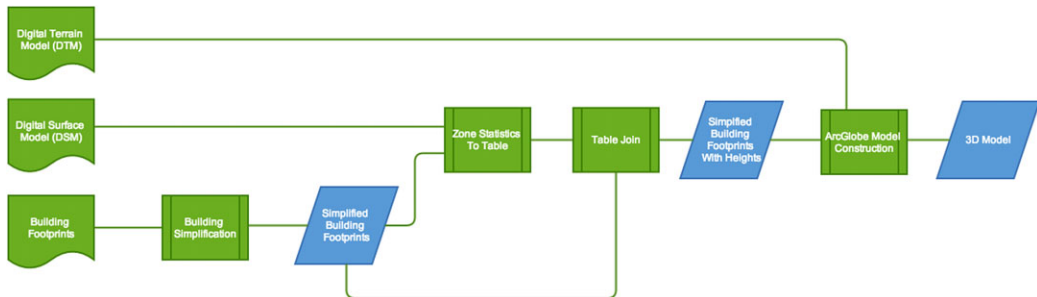


Figure 9 Process flow diagram of 3D modeling objective

The last parameter to run the tool was the calculated statistic for each region. With the study area representing the Downtown core of San Francisco, the vast majority of roofs will be relatively flat, with some variations due to auxiliary features such as door landings, exhaust fans, and elevated roof edges. Due to this characteristic of the buildings in the downtown region, the statistics selected to represent the overall height of the building was the mean height statistic. The majority and median statistics also presented viable alternatives for calculating the building height, but the mean was selected to equalize potentially minor variations in building height. Running the tool, a table of mean values for building heights was calculated for each zone. The resulting table was then joined to the original building footprint shapefile based on the common ID attribute. This approach was influenced and extended from the work of Elaksher and Bethel (2004), who used a kernel pixel approach and DEM raster to identify pixels with large variations in height among adjacent pixels, and therefore were able to identify building footprints and associated building heights (Elaksher and Bethel 2002).

2.4.2 Building footprint simplification

The next step that was required in the construction a 3D model was to refine the extracted building footprint due to the large amount of edge variation present as a result of the resolution of the imagery and the method used to extract the footprint. These complexities resulted in poor model performance and an overall lower quality representation of our results. To refine the building footprints for better visual experience when projected in a 3D model, The Building Simplification tool within ArcGlobe was used to approximate the underlying geometric qualities of each building. The tool required a single input shapefile of the extracted building footprints and contained a single parameter of the simplification tolerance. A set of numbers ranging from 1 to 250 were inputted as the simplification tolerance with a varying degree of success in representing the underlying geometric patterns. Figure 10 displays tolerances set for the building simplification step.

Although the varying accuracy in representing the geometric features of the building varies with each tolerance value, for the visual communication of the model through the 3D model, a tolerance value of 250 meter was selected. This value was derived by locating the largest wall segment in the scene and measuring the distance to attain a simplification tolerance. Visually comparing the accuracy of the extracted footprints, the simplified footprints, and the city plan in Figure 11, the simplification of the building footprints was justified as the model will serve to place more emphasis on the visual communication of PV potential rather than building accuracy.

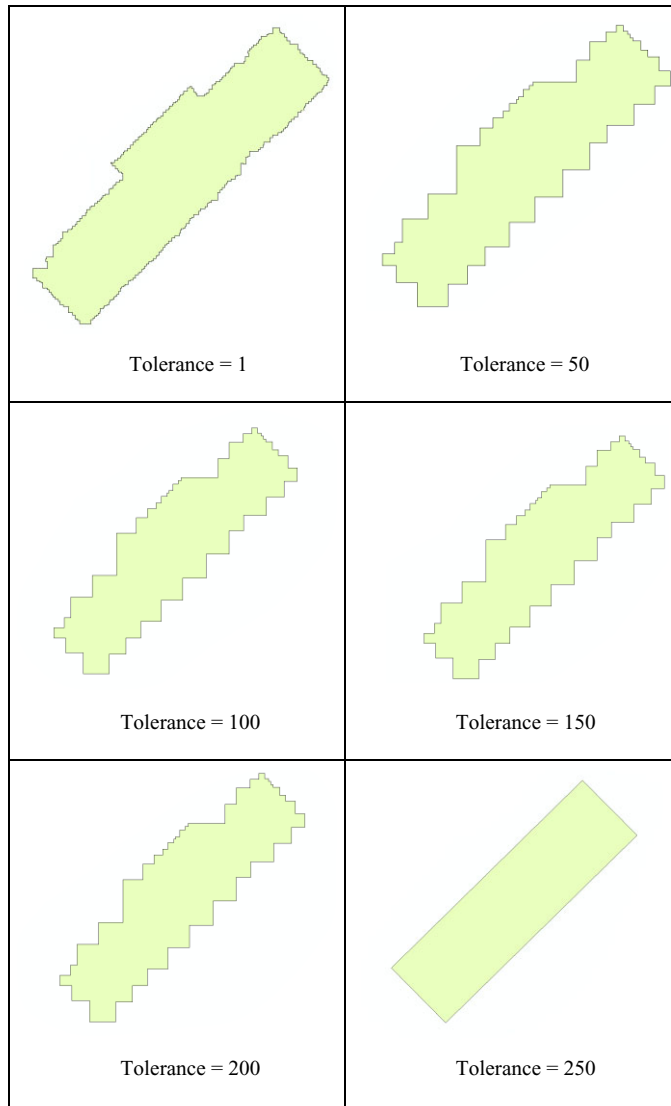


Figure 10 Building simplification at various simplification tolerances

2.4.3 Developing 3D model

Using these datasets, a 3D model of the study area was constructed using ArcGIS's ArcGlobe modeling platform. Within ArcGlobe, there were a number of important layer concepts specific to modeling 3D environments that need to be considered. Elevation layers form the base of the model, and represent the elevation of underlying terrain features. Draped layers represent features placed upon an established base elevation layer. The last layer to consider is the floating lower level which has a defined height attribute to exist in space without direct contact with surface features (<http://help.arcgis.com/en/arcgisdesktop/10.0/help/index.html#/00q8000000zp000000>). Modeling an urban environment, the elevation layer serves as the key layer to model the surface of the Earth, and the draped layer serves to represent the building

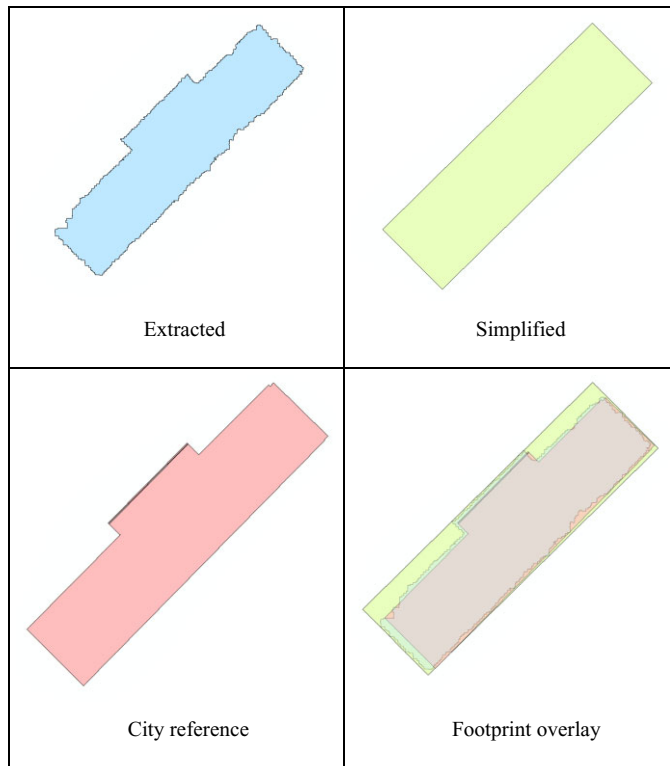


Figure 11 Building footprint simplification comparison

footprints, placed upon the non-uniform surface model. The dataset that was used to model the terrain surface was the digital terrain model (DTM) raster representing the varying elevation of the Earth's surface within the study area. The extracted building footprint dataset was used as the draped layer, representing the outline of the buildings upon the elevation model.

To build a 3D representation of the buildings, the globe extrusion property of the building footprint layer was used. The extrusion turns points into vertical lines, lines into walls, and polygons into block polygons. The attribute value that was used as the extrusion expression was the calculated mean height of the building footprints, and the extrusion was applied from the minimum height of the elevation directly under the footprint. Figure 12 represents the extruded building footprints of all the buildings within the study area.

The final step of the 3D model construction is to represent each building's PV potential by coloring each building polygon by its PV potential value. Within the layer properties, a graduated symbology was applied using seven classes that represent the range of PV values across the study area. Figure 13 shows the resulting 3D representation of the study area, with extruded building polygons and PV potential symbology applied.

3 Results

3.1 Building Footprint

The first result was the building footprint (Figure 14). There were 168 building polygons. In Figure 14, most buildings were extracted correctly from the original building height image.

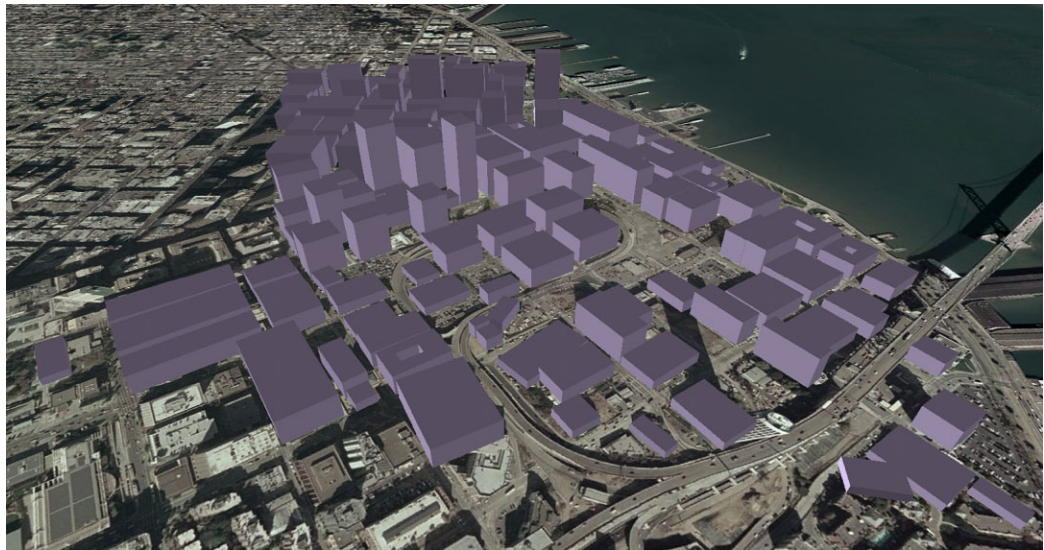


Figure 12 Extruded building footprints by mean height

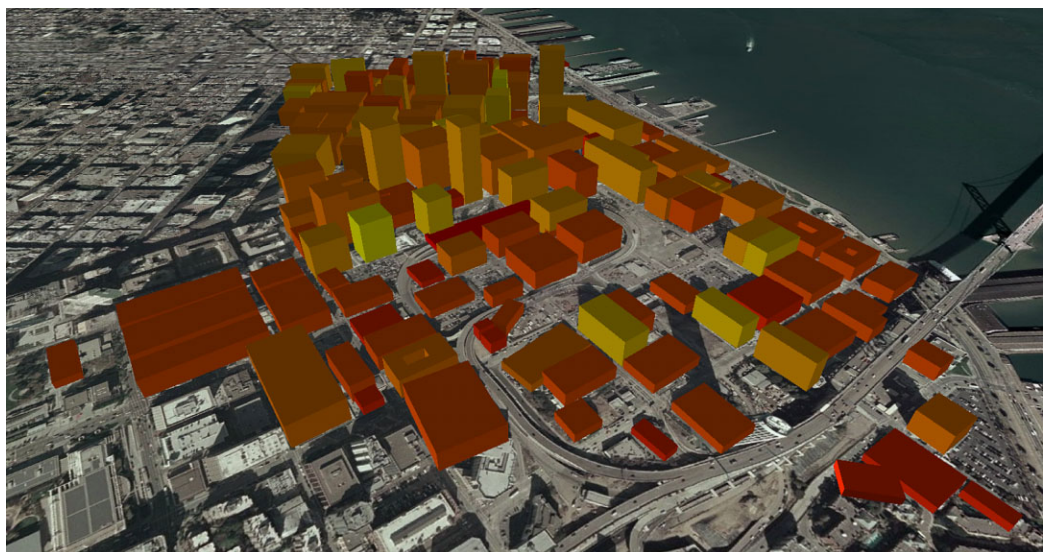


Figure 13 3D model of Downtown San Francisco with extruded building footprints and yearly PV potential symbology applied

Most of the extracted buildings have rectangular shapes and appropriate sizes. However, some of them were of irregular shapes and did not look like buildings. There were also several buildings situated at the edge of the study area and parts of them were cut off by the image.



Figure 14 Building footprints

3.2 Solar Irradiation

3.2.1 Yearly sum of solar irradiation

Figure 15 shows the yearly sum of solar irradiation (pixel-based) from a series of daily maps. The pixel-based map shows the detailed solar irradiation information. The more red the pixel is, the more solar radiation it receives. The more yellow the pixel is, the less solar radiation it receives. The highest pixel value is 2,586 kWh/m², while the lowest pixel value is 183 kWh/m². The variability of solar irradiation is large both through the map and within each building. For example, in Figure 16, the left-hand building shows large variations in terms of the pixels' solar irradiation values. Low solar irradiation pixels are located on the edges of the building. High value pixels were clustered within the middle of the building in a rectangular shape. However, for the right-hand building, pixels have highly uniform values with a low standard deviation. When performing average function in terms of building footprints, the left building would have lower PV potential compared with the right building.

The yearly sum of solar irradiation map (building-based) was zoned on the top of yearly sum of solar irradiation map (pixel-based) which is shown as Figure 17. Buildings with red colors have high solar irradiation, whereas buildings with yellow colors have low solar irradiation. From Table 3, the highest value of solar irradiation among all buildings is approximately 2,110 kWh/m², and the lowest is approximately 967 kWh/m². The mean value and the median value are 1,675 kWh/m² and 1,718 kWh/m² respectively with the standard deviation of 239.4 kWh/m².

Solar irradiation values were categorized into seven levels with an increment of 200 kWh/m²: level 1 (900–1,100), level 2 (1,100–1,300), level 3 (1,300–1,500), level 4 (1,500–1,700), level 5 (1,700–1,900), level 6 (1,900–2,100), and level 7 (2,100–2,300). Figure 18 shows that the majority of buildings fall within the fifth class, with 65 buildings having solar irradiation

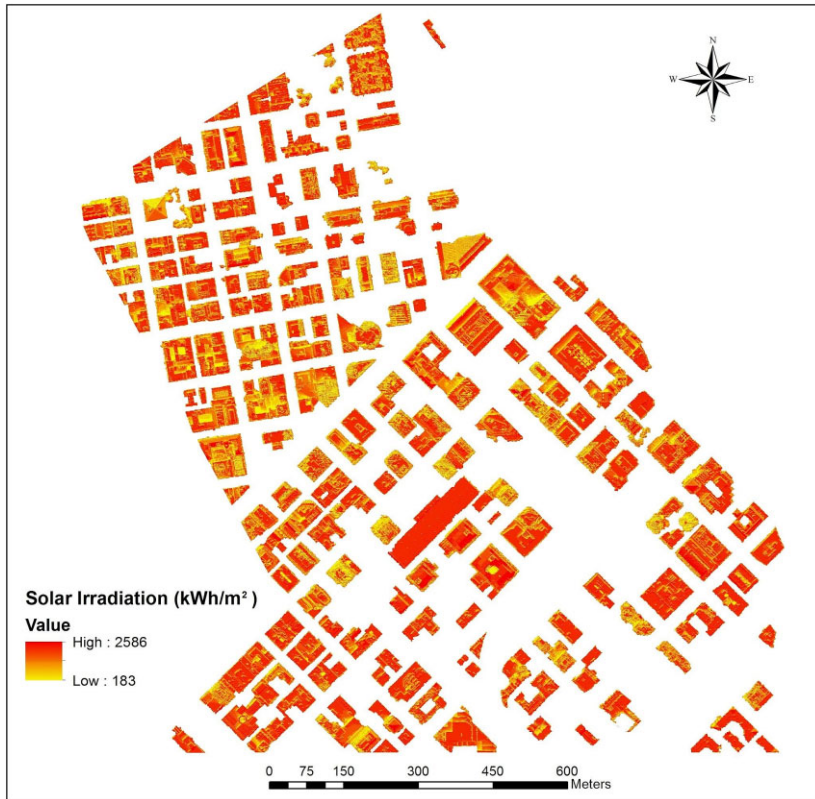


Figure 15 Yearly sum of solar irradiation map (pixel-based)

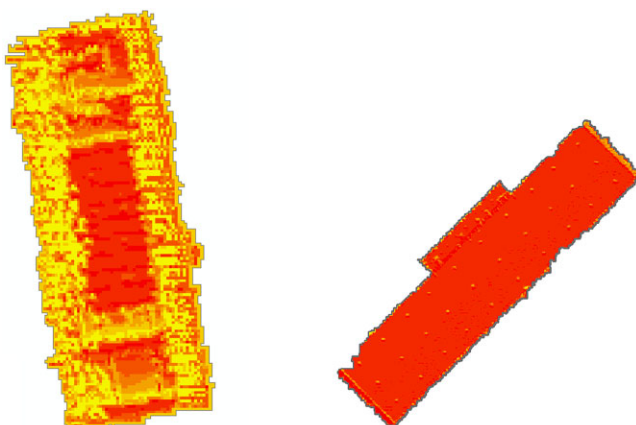


Figure 16 Sample buildings showing solar irradiation variations within building boundaries



Figure 17 Yearly sum of solar irradiation map (building-based)

Table 3 Descriptive statistics of yearly sum of solar irradiation

N	Max (kWh/m ²)	Min (kWh/m ²)	Mean (kWh/m ²)	Median (kWh/m ²)	SD (kWh/m ²)
168	2,110	967	1,675	1,718	239.4

between 1,700–1,900 kWh/m². Only one building and three buildings are in levels 7 and 1, respectively. High PV potential buildings are distributed without an obvious pattern. However, several red clusters can be identified such as the left bottom corner, the right bottom corner and the top middle parts of the study area.

3.2.2 Monthly sum of solar irradiation

The monthly sum of solar irradiation values was categorized into seven levels with an increment of 30 kWh/m²: level 1 (45–75), level 2 (75–105), level 3 (105–135), level 4 (135–165), level 5 (165–195), level 6 (195–225), and level 7 (225–255). The higher the level, the more red the building is, the lower the level the more yellow the building is. From the 12-month solar radiation map series (Figure 19), it can be seen that the irradiation of the extracted buildings

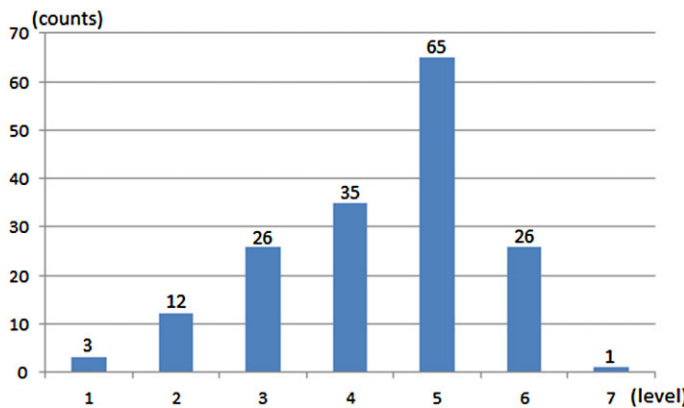


Figure 18 Histogram of building counts and corresponding solar irradiation levels

stays at a relatively low level in January and February. Starting from March, solar irradiation increases gradually until it reaches the peak between May and July. Then the irradiation begins to decrease and reaches the lowest level in December. The monthly solar irradiation values follow an obvious yearly cycle.

4 Discussion

4.1 Building Footprint Evaluation

The object-extracted building footprint (Figure 14) was compared with the San Francisco City building footprint (Figure 20) to validate the accuracy of the footprint generated in this project qualitatively. By overlaying the two footprints (Figures 21 and 22), it could be visualized that most of the buildings were successfully extracted since they match the San Francisco city footprint quite well. However, the City of San Francisco data contains more fine details of building structures. Figure 23 showed the same building in the two footprint data sets. It was clear that the city footprint divided the buildings into several smaller blocks, while the object-extracted building provided less information. In the extracted footprint image, there were also some areas (e.g. Figure 24) that had much lower accuracy than other areas. In Figure 24, four areas were numbered and highlighted using red squares. The figure compared the extracted building footprint with the San Francisco footprint, using Google Maps satellite image for verification. In area 1, there were some tree-shaped buildings in the extracted footprint but not in the San Francisco city data. This area is actually a park in Google map. This misclassification happened because trees sometimes can be as high as buildings and when a tree has dense canopy, it might have similar LiDAR first returns as a building. In areas 2, 3, and 4, the extracted footprints missed parts of the buildings which should exist as shown in Google map. Examining Figure 25, it was found that all these building pieces have very low height (around 8 m). Considering that the surrounding buildings have heights of up to 70 m, these missed buildings do not seem to have much PV potential. Thus, it can still be concluded that the extracted footprints are of high quality.

4.2 PV Analysis

The yearly sum of solar irradiation map shows the PV potential pattern through the downtown center of San Francisco. The yearly average solar irradiation on a horizontal surface

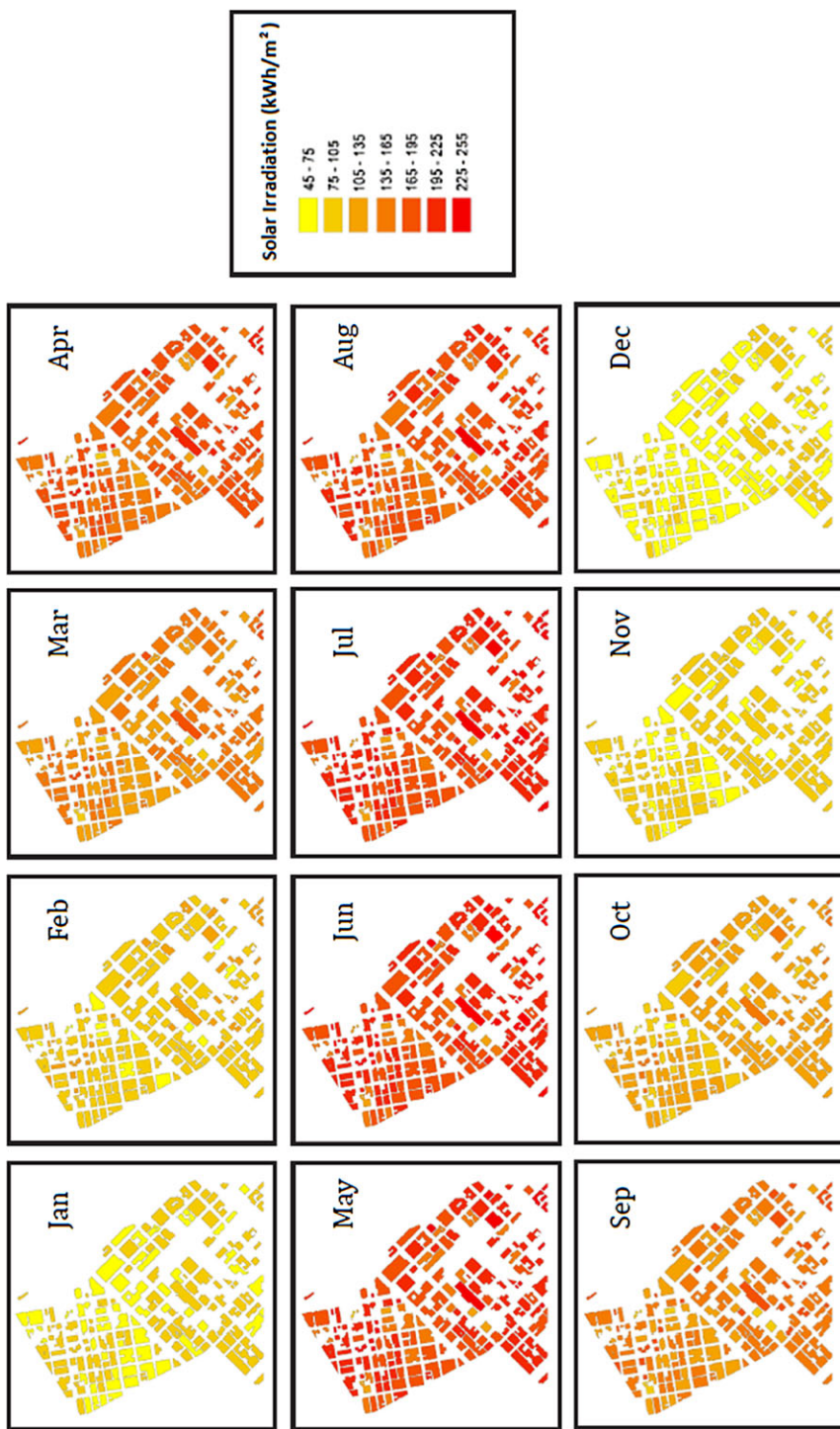


Figure 19 Monthly sum of solar irradiation



Figure 20 San Francisco building footprint (Retrieved from <https://data.sfgov.org/>)

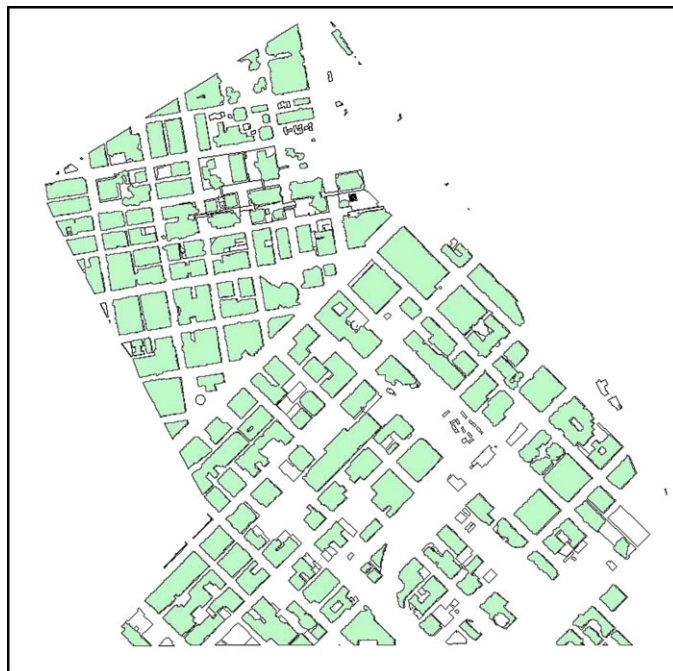


Figure 21 Overlay of two footprints: extracted footprint (green) on San Francisco City data (white)



Figure 22 Overlay of two footprints: San Francisco City data (white) on extracted footprint (green)

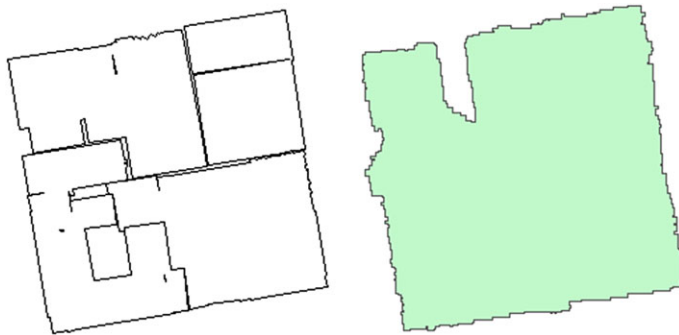


Figure 23 Building footprints: San Francisco City data (left) and extracted footprint (right)

under clear-sky conditions is $1,675 \text{ kWh/m}^2$. The estimated yearly value was compared with data retrieved from the NASA Langley Research Center Atmospheric Science Data Center Surface meteorological and Solar Energy (SSE) web portal supported by the NASA LaRC POWER Project, where a global 1 degree grid of solar radiation data are provided. In 2004, the yearly sum of solar irradiation on a horizontal surface under clear-sky conditions is $1,692.48 \text{ kWh/m}^2$ for the grid (centered on 37.5° N , -122.5° W), which is approximately equal to the value estimated in the study.

When comparing PV potential among buildings, it was assumed that high buildings tend to have relatively high solar irradiation values because they are free of or less sensitive to shadowing effects. However, the building with highest solar irradiation ($2,110 \text{ kWh/m}^2$) is the new

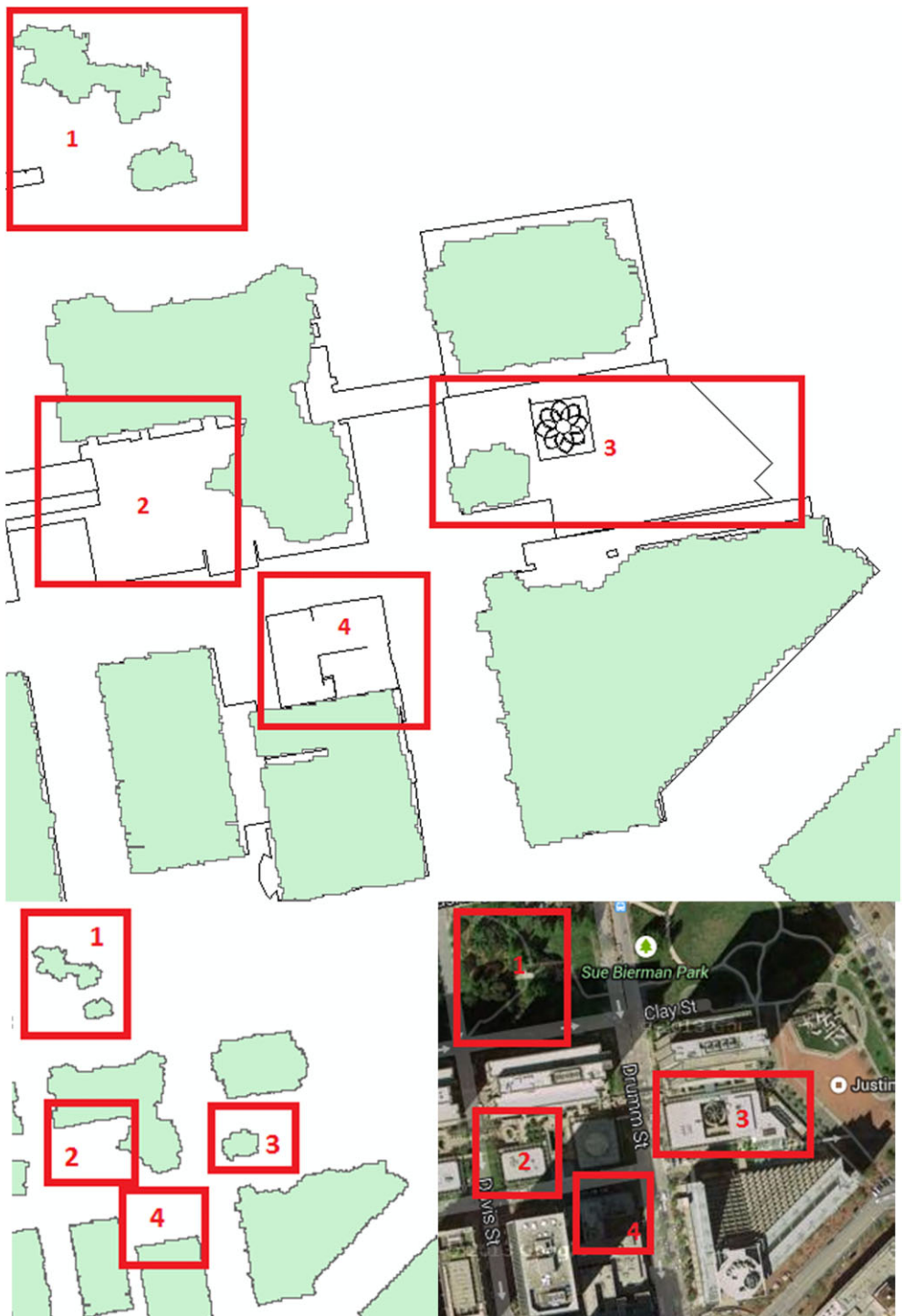


Figure 24 Problem area: San Francisco City data (white), extracted footprint (green), and Google Maps satellite image



Figure 25 Problem area (building height image)

SF Transbay Terminal with a mean height of 13.1 m. In addition, the highest building (555 Mission St.) with a mean height of 159.3 m has yearly solar irradiation of 1,444 kWh/m², which is below the average level. The previous assumption, that the building height might be a significant determinant of PV potential, was then questioned.

When looking at pixel-based solar irradiation, it was found (Figure 26) that the highest building is very fuzzy with huge variation of solar irradiation values, while the highest PV potential building has consistent solar irradiation values. In Google Maps, the highest building was found to have irregular edges and several signal receivers which would cast shadows on the top of the building. Whereas the highest PV potential building is flat without obvious surface features. Another hypothesis is that the flatness of the building roof might be a possible determinant of PV potential, and it should be tested in a statistical model.

Therefore, three variables that might influence the building PV potential were considered: building height, roof complexity, and roof area. The three factors were tested using a multiple regression model. The roof complexity of a building was represented by the standard deviation of the height of the points within the building roof. The values of the three factors were first reclassified into three new groups, each of which contains only two unique labels, that is, “high” and “low”, respectively. In the result, large P-value for variables area (0.45) and height (0.19) shows that these two factors do not make significant contribution in the regression

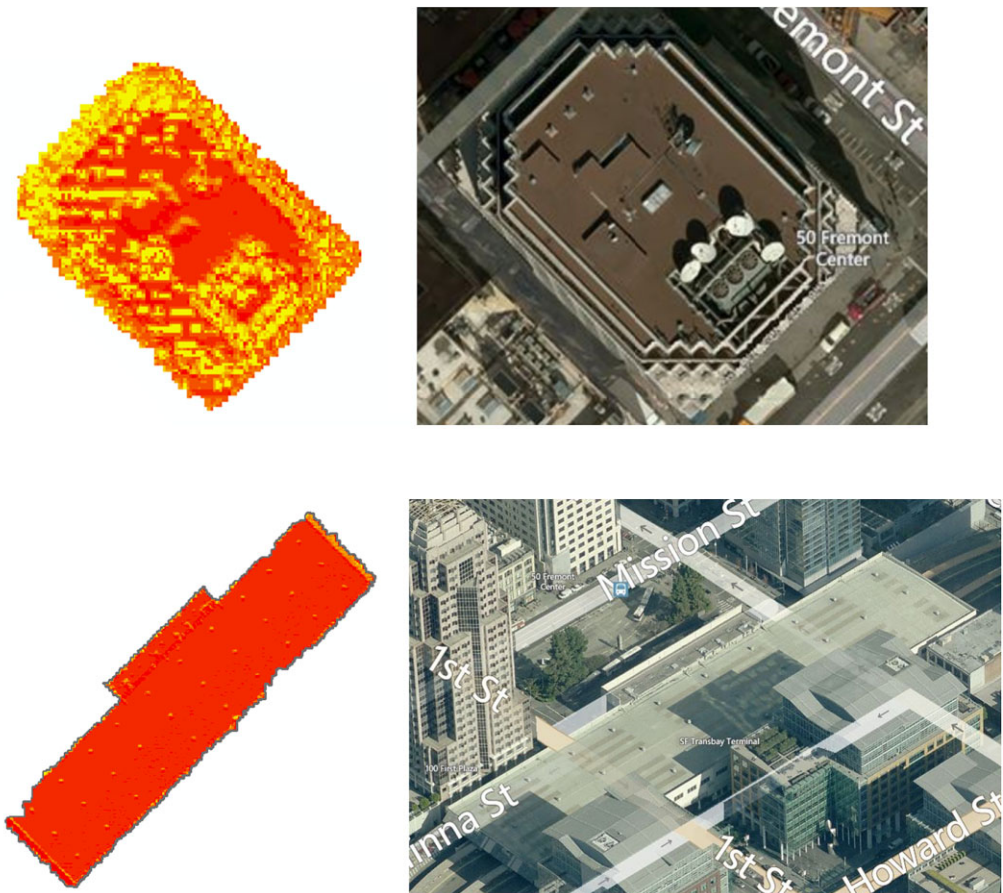


Figure 26 Highest building versus highest PV potential building

model, and those two variables were deleted from the model. The building height was expected to be a significant factor but actually not. One possible explanation is that the height of each building was considered independently instead of taking the shadowing effect of the surrounding buildings into account. When performing simple regression of solar radiation on building roof complexity factor solely, it showed that 43.9% of the variation among these buildings was explained. Comparing the yearly sum of solar radiation map (Figure 17) with the roof complexity map (Figure 27), it could be seen that buildings with complex roofs tend to have low PV potential. The regression equation showed:

$$\text{PV potential} = 1845.7 - 9.14 \text{ Roof Complexity} \quad (2)$$

4.3 3D Model

The construction of a 3D model carried with it a number of simplifying steps that helped communicate the overall skyline of Downtown San Francisco more effectively and increase the performance of the overall model in representing PV potential. Figure 28 displays a comparison

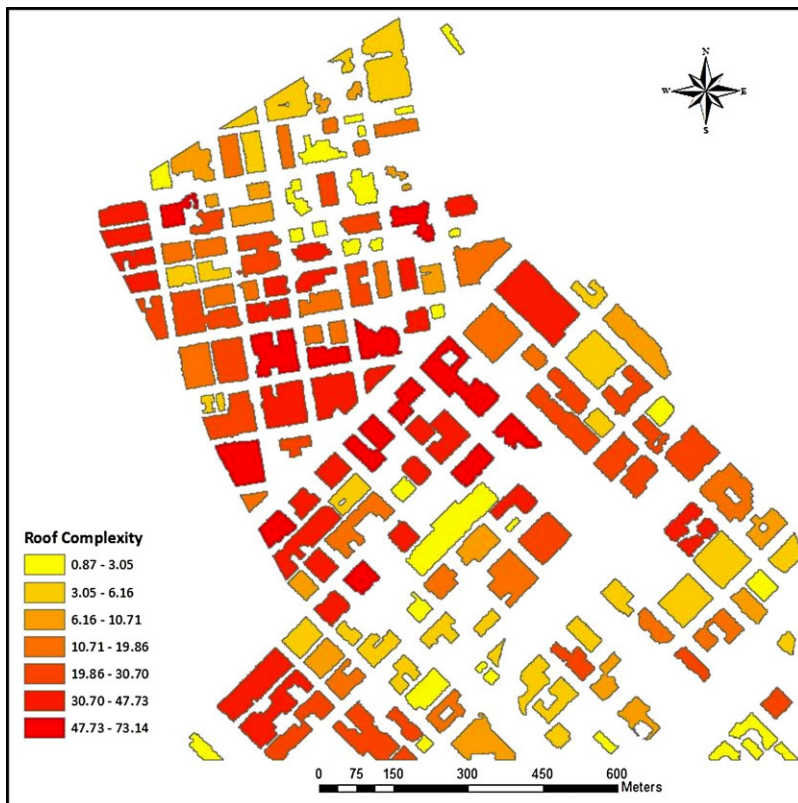


Figure 27 Roof complexity map

of the resulting models, taken from the same perspective, to represent the impact the simplification step had on the overall representation of the model. The overall shapes of the buildings are represented with a higher degree of accuracy without running the Building Simplification tool, but when extruding the building footprints into 3D, a number of visual artifacts resulted in a less esthetically pleasing representation of the skyline. These artifacts detract from the power of the 3D representation by placing more emphasis on the accuracy of the footprints than the symbology of the PV potential for each building. The simplification step was a design choice within the scope of this research, to better communicate the results of the PV potential, and overall resulted in a better visual experience in the model.

4.4 Limitations

4.4.1 Uncertainties in *r.sun* model

The *r.sun* solar irradiation model used in this study is complex and flexible, and it has a sound theoretical background presented in the ESRA research projects. The model's inherent limitations are due to the estimation algorithms in that project. Also, the *r.sun* is designed to map large-scale areas with high terrain heterogeneity, but it is easy to transfer into regional studies (Šúri and Hofierka 2004). However, few studies had focused on building scale so far, therefore detailed limitations are not well documented in the literature. What can be identified is that

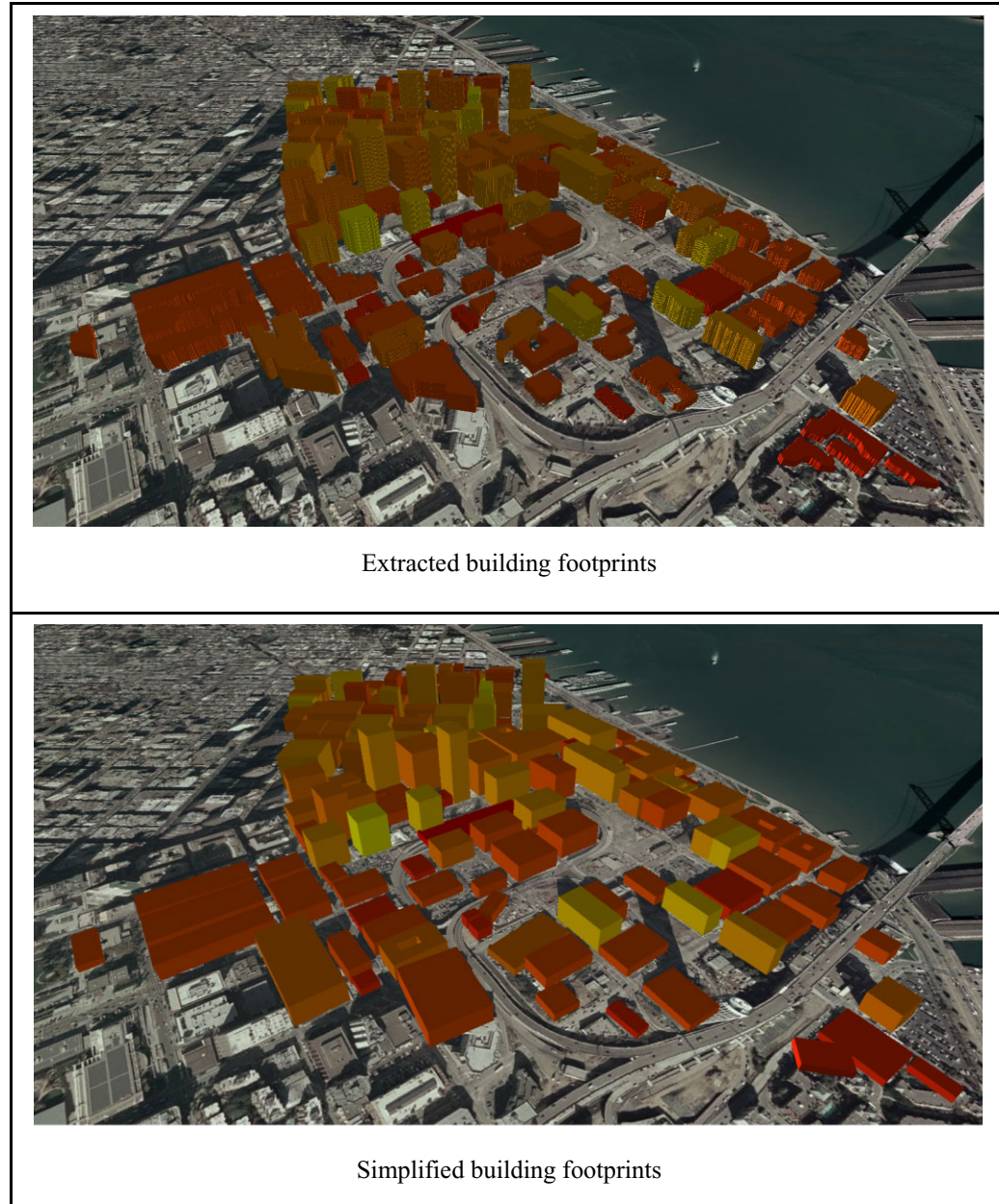


Figure 28 Comparison of 3D models with extracted and simplified building footprints

the main limitation of the model is the limitation of the data source. The ambiguity regarding building footprints and detailed surface information leads to uncertainties in solar irradiation computation. What is more, the atmospheric information (Linke Turbidity Factor, used; clear-sky index, unused) is limited temporally and spatially. Thus, it is important to interpret the results of *r.sun* as a tentative estimation of the future PV potential.

4.4.2 The boundary problem

The boundary problem is a potential source of uncertainty in this research. In spatial analysis, the boundary problem happens when lacking neighbors in analysis which depends on the values of the neighbors (Burt et al. 2009). In this study, buildings that are located outside the study area were excluded from the analysis. However, since the *r.sun* model takes shadowing effects into account, the neighboring tall buildings, if they exist, are expected to cast shadows on buildings within the study area. Under this circumstance, buildings within the study area but close to the boundary may have lower PV potential, and buildings around the center of the study area should have more accurate estimates. Surrounding buildings located outside the study area were examined in terms of their heights, using Bing Map 3D Bird's Eye product. The result shows that the study area was well chosen, and most high buildings were included in the study area. Only a few high buildings are situated out of the study area, and their shadowing effects are not considerable.

4.4.3 Building footprint spatial conflicts

The Building Simplification tool was a valuable component in the construction of the 3D model of the Downtown region of San Francisco to visually communicate the overall skyline. The tool, however, created occasional spatial conflicts that were logged and identified when the tool was run. Figure 29 shows an occurrence of such a spatial conflict in the 3D model, in comparison to the extracted building footprint. Within the scope of this project, these spatial conflicts were not corrected as each building footprint still effectively represented the overall PV potential. However, future research in constructing a more accurate representation of the buildings will mediate these spatial conflicts by logging and addressing each spatial conflict as it occurs, through either manual or automated techniques.

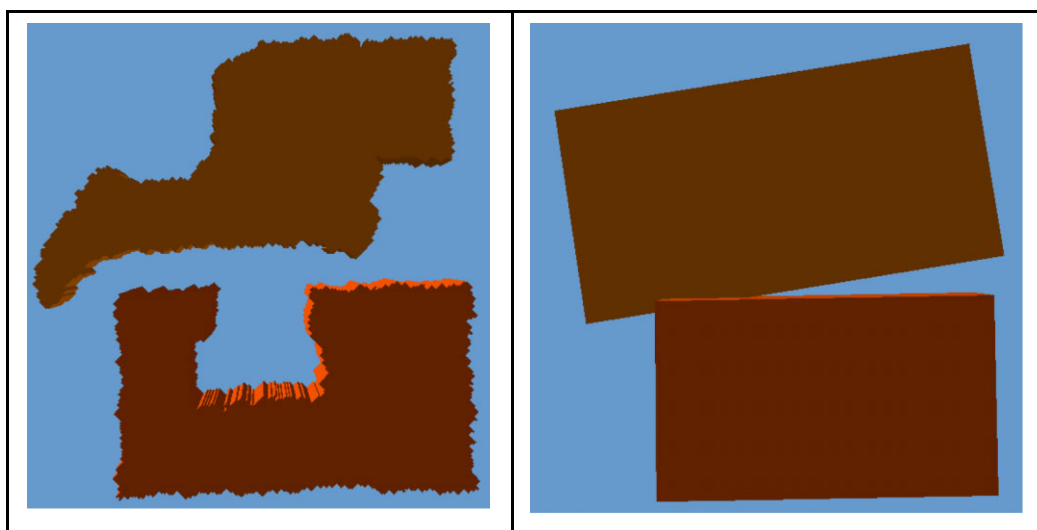


Figure 29 Comparison of extracted building footprint and simplified footprint showing resulting spatial conflicts

4.4.4 Height uncertainty

In the construction of a 3D model of Downtown San Francisco, the scope of the 3D visualization was to provide a more effective visualization of PV potential for decision makers. Although the visualization provided a fairly high quality representation of the results of our research, the visualization carries with it an inherent uncertainty in scale and magnitude of the actually building heights. This uncertainty arises from the methodology used to calculate the building heights under the assumption that the Downtown region of San Francisco has buildings that have fairly flat roof areas. This assumption was used to average out the height variation of all the building pixels in the DSM raster and calculated the overall building height for the building footprint. This assumption, however, might not be true for all buildings and in some cases buildings might contain auxiliary components on the roof that create an added level of uncertainty in the construction of an accurate 3D representation of the city. These uncertainties can be accounted for and largely addressed through future research and work as described in the subsequent section.

4.4.5 Unexplained R^2

As discussed in previous sections, the simple regression model only explained 43.9% of the building PV potential variations. The model solely considered the roof complexity factor. Building height, which might be an important influence factor, was regarded as non-significant. Building surroundings were also not included in the regression model. If a building is surrounded by high buildings, solar radiation to this building might be blocked by the building shadows. Thus, another factor, “building population”, should be defined and input to the regression model. In addition, the sea-level altitude might be a significant factor since a relatively low building can have high altitude if the slope of the region varies greatly. This factor could be calculated using DSM data.

4.5 Future Work

In the future, the methodology presented in this research can be fully automated. Solar irradiation simulation in GRASS was performed in shell scripts in this study, but it can also be integrated with Python. Additionally, 3D modeling in ArcGIS is able to be transformed into Python with the ArcGIS Python Package. Although the object-oriented classification to extract building footprint is hard to plant outside of eCognition, one alternative is to use the existing building footprints archive data, which can be created from digitizing or surveying. One concern is the availability of high resolution LiDAR data, specifically to create a high quality DEM. The possible solution is to replace this need with Global DEMs (GTOPO30 and SRTM3), which were used in Nguyen and Pearce’s study in 2010. Then, the building height information from the city’s building footprints can be overlaid with the DEM to generate a surrogate DSM which can be input into the *r.sun* model for further simulation. Once the whole process is automated, the method can be generalized to cities and not limited to San Francisco.

Additionally, in this study, solar radiation on horizontal surface under clear-sky condition is of the interest to quantify geographical PV potential. Future work can integrate meteorological station records in terms of weather conditions for real-sky simulation. Also, it would be a good idea to expand the geographical PV potential at a higher level considering technical, economic and social aspects (Hoogwijk 2004; Izquierdo et al. 2008).

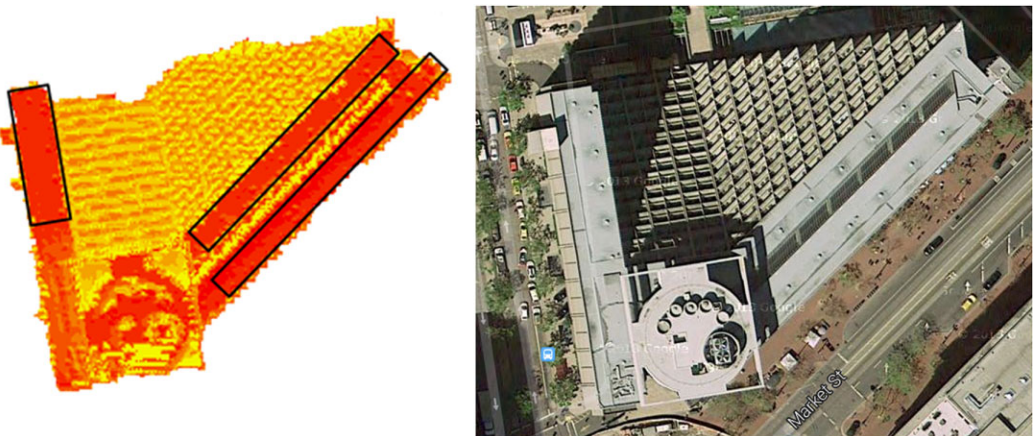


Figure 30 Potential solar panel positions on Hyatt Regency San Francisco

Furthermore, a potential direction for further research in estimating solar PV potential might be to augment the efforts in estimating solar PV potential not just by extracting the building footprints, but by further segmenting the region into distinct subregions that can more effectively represent a building roof. Forlani et al. (2006) propose a two-stage classification approach to further segment building roof regions by first outlining the root region edges, then identifying distinct subregions such as roof slope, root outlines, and noise objects such as substructures, chimneys, or vegetation. Further, Tse et al. (2008) propose that a mesh of Delaunay triangles be constructed for roof regions, and the normal to each triangle is averaged in either a 2D (unit semicircle) or 3D (unit hemispherical) manner, and compared to other roof regions to identify contiguous roof regions with similar orientations. Utilizing either of these techniques in conjunction with the solar irradiation simulation could potentially yield a better representation of building rooftops, and subsequently lead to more accurate PV potential estimates.

Another possible approach to selecting high PV potential area for installing PV panels on buildings is to apply object oriented classification upon the pixel-based yearly sum of a solar irradiation map. For example, in Figure 30, high potential parts were marked with black lines on the Hyatt Regency San Francisco. Those parts can be identified using the object-oriented classification method through a series of rules considering the standard deviation and mean of solar irradiation, shape and minimum area. Then if the marked area can be classified and identified, those parts can be ideal positions to place solar panels.

5 Conclusions

In this experiment, the LiDAR image was much better for building extraction than optical satellite imagery. The r.sun model was shown to be a feasible approach to estimate PV potential at the building scale. Solar radiation values for each building calculated over a one year cycle and there were obvious variations among different months. The yearly sum of solar radiation for each building ranged from 967 to 2,110 kWh/m². The geographical PV potential of a building was influenced by the building roof complexity. Buildings with simple and smooth building roofs tend to have higher PV potential than those buildings with complex roofs.

Uncertainties in the study mostly resulted from the image boundary effect and the accuracy of LiDAR data and extracted building footprints. Future work can be done to automate the PV modeling process so it can be utilized outside the San Francisco city.

References

- Adelaja S, Shaw J, Beyea W, and McKeown J D 2010 Renewable energy potential on brownfield sites: A case study of Michigan. *Energy Policy* 38: 7021–30
- Angelis-Dimakis A, Biberacher M, Dominguez J, Fiorese G, Gadocha S, Gnansounou E, and Robba M 2011 Methods and tools to evaluate the availability of renewable energy sources. *Renewable and Sustainable Energy Reviews* 15: 1182–200
- Baatz M and Schäpe A 2000 Multiresolution segmentation: An optimization approach for high quality multi-scale image segmentation. *Angewandte Geographische Informationsverarbeitung* 12: 12–23
- Boyle G 2004 *Renewable Energy*. New York, Oxford University Press
- Burt J E, Barber G M, and Rigby D L 2009 *Elementary Statistics for Geographers*. London, Guilford Press
- Carneiro C, Morello E, and Desthieux G 2009 Assessment of solar irradiance on the urban fabric for the production of renewable energy using LiDAR data and image processing techniques. In Sester M, Bernard L, and Paelke V (eds) *Advances in GIScience: Proceedings of the Twelfth AGILE Conference*. Berlin, Springer Lecture Notes in Geoinformation and Cartography: 83–112
- City and County of San Francisco 2006 Visitors: San Francisco Historical Information. WWW document, http://web.archive.org/web/20060301022510/http://sfgov.org/site/visitor_index.asp?id=8091
- City and County of San Francisco 2014 San Francisco Solar Map. WWW document, <http://sfenergymap.org>
- Dubayah R and Rich P M 1995 Topographic solar radiation models for GIS. *International Journal of Geographical Information Systems* 9: 405–19
- Duffie J A and Beckman W A 1991 *Solar Engineering of Thermal Processes*. New York, John Wiley and Sons
- Elaksher A F and Bethel J S 2002 Reconstructing 3D buildings from LiDAR data. *International Archives of Photogrammetry Remote Sensing and Spatial Information Sciences* 34(3/A): 102–7
- Fischer A, Kolbe T H, Lang F, Cremer A B, Förstner W, Plümer L, and Steinhage V 1998 Extracting buildings from aerial images using hierarchical aggregation in 2D and 3D. *Computer Vision and Image Understanding* 72: 185–203
- Forlani G, Nardinocchi C, Scaioni M, and Zingaretti P 2006 Complete classification of raw LiDAR data and 3D reconstruction of buildings. *Pattern Analysis and Applications* 8: 357–74
- Haala N and Brenner C 1999 Extraction of buildings and trees in urban environments. *ISPRS Journal of Photogrammetry and Remote Sensing* 54: 130–37
- Hetrick W A, Rich P M, Barnes F J, and Weiss S B 1993 GIS-based solar radiation flux models. In *Proceedings of the American Society of Photogrammetry and Remote Sensing Annual Conference*, New Orleans, Louisiana: 132–43
- Hofierka J and Šúri M 2002 The solar radiation model for Open source GIS: Implementation and applications. In *Proceedings of the Open Source GIS-GRASS Users Conference*, Trento, Italy
- Hofierka J and Kaňuk J 2009 Assessment of photovoltaic potential in urban areas using open-source solar radiation tools. *Renewable Energy* 34: 2206–14
- Hoogwijk M M 2004 On the Global and Regional Potential of Renewable Energy Sources. Unpublished PhD Dissertation, University of Utrecht
- Ineichen P and Perez R 2002 A new airmass independent formulation for the Linke turbidity coefficient. *Solar Energy* 73: 151–57
- Izquierdo L R, Galán J M, Santos J I, and Olmo R D 2008 Modelado de sistemas complejos mediante simulación basada en agentes y mediante dinámica de sistemas. *Empiria: Revista de Metodología de Ciencias Sociales* 16: 85–112
- Jochum A, Höfle B, Rutzinger M, and Pfeifer N 2009 Automatic roof plane detection and analysis in airborne LiDAR point clouds for solar potential assessment. *Sensors* 9: 5241–62
- Kassner R, Koppe W, Schüttenberg T, and Bareth G 2008 Analysis of the solar potential of roofs by using official LiDAR data. *International Archives of the Photogrammetry, Remote Sensing and Spatial Information Sciences* 37(B4): 399–404
- Kasten F 1996 The Linke turbidity factor based on improved values of the integral Rayleigh optical thickness. *Solar Energy* 56: 239–44
- Li W, Li L, Goodchild M F, and Anselin L 2013 A geospatial cyberinfrastructure for urban economic analysis and spatial decision-making. *ISPRS International Journal of Geo-Information* 2: 413–31

- Liang J, Gong J, Li W, and Ibrahim A N 2014 A visualization-oriented 3D method for efficient computation of urban solar radiation based on 3D–2D surface mapping. *International Journal of Geographical Information Science* 28: 780–98
- Liu Y, Li M, Mao L, Xu F, and Huang S 2006 Review of remotely sensed imagery classification patterns based on object-oriented image analysis. *Chinese Geographical Science* 16: 282–8
- Liu J and Wu J 2010 *Multi-agent Robotic Systems*. Boca Raton, FL, CRC Press
- Meinel G and Neubert M 2004 A comparison of segmentation programs for high resolution remote sensing data. *International Archives of Photogrammetry, Remote Sensing and Spatial Information Sciences* 35(B4): 1097–102
- Mészáros P, Rees M J, and Wijers R A M J 1998 Viewing angle and environment effects in gamma-ray bursts: Sources of afterglow diversity. *Astrophysical Journal* 499: 301–8
- Moons T, Frere D, Vandekerckhove J, Van Gool L, Leuven K U, and Psi E 1998 Automatic modelling and 3D reconstruction of urban house roofs from high resolution aerial imagery. In *Proceedings of the Fifth European Conference on Computer Vision*, Freiburg, Germany: 410–25
- Nguyen H T and Pearce J M 2010 Estimating potential photovoltaic yield with r.sun and the open source Geographical Resources Analysis Support System. *Solar Energy* 84: 831–43
- Nguyen H T and Pearce J M 2012 Incorporating shading losses in solar photovoltaic potential assessment at the municipal scale. *Solar Energy* 86: 1245–60
- Pearce J 2002 *Civil Society and Development: A Critical Exploration*. Boulder, CO, Lynne Rienner Publishers
- Rigollier C, Bauer O, and Wald L 2000 On the clear sky model of the ESRA-European Solar Radiation Atlas, with respect to the Heliosat method. *Solar Energy* 68: 33–48
- Rottensteiner F and Briese C 2002 A new method for building extraction in urban areas from high-resolution LIDAR data. *International Archives of Photogrammetry Remote Sensing and Spatial Information Sciences* 34(3/A): 295–301
- Rottensteiner F and Briese C 2003 Automatic generation of building models from LIDAR data and the integration of aerial images. *International Archives of the Photogrammetry, Remote Sensing and Spatial Information Sciences of the ISPRS* 34(3/W13): 174–80
- Scharmer K and Greif J (eds.) 2000 *The European Solar Radiation Atlas* (Volume 1). Paris, France, Presses des Mines
- Shackelford A K, Davis C H, and Wang X 2004 Automated 2-D building footprint extraction from high-resolution satellite multispectral imagery. In *Proceedings of the IEEE International Geoscience and Remote Sensing Symposium*, Beijing, China
- Sohn G and Dowman I 2007 Data fusion of high-resolution satellite imagery and LiDAR data for automatic building extraction. *ISPRS Journal of Photogrammetry and Remote Sensing* 62: 43–63
- Šúri M and Hofierka J 2004 A new GIS-based solar radiation model and its application to photovoltaic assessments. *Transactions in GIS* 8: 175–90
- Šúri M, Huld T A, and Dunlop E D 2005 PV-GIS: A web-based solar radiation database for the calculation of PV potential in Europe. *International Journal of Sustainable Energy* 24(2): 55–67
- Syed S, Dare P, and Jones S 2005 Semi-automatic 3D building model generation from LiDAR and high resolution imagery. In *Proceedings of Spatial Intelligence, Innovation and Praxis: The National Biennial Conference of the Spatial Sciences Institute*, Melbourne, Australia
- Tse R O C, Gold C, and Kidner D 2008 3D city modelling from LIDAR data. In van Oosterom P, Zlatanova S, Penninga F, and Fendel E (eds) *Advances in 3D Geoinformation Systems*. Berlin, Springer Lecture Notes in Geoinformation and Cartography: 161–75
- US Census Bureau 2012 San Francisco (city), California. WWW document, <http://quickfacts.census.gov/qfd/states/06/0667000.html>
- Zhou Q-Y and Neumann U 2008 Fast and extensible building modelling from airborne LiDAR data. In *Proceedings of the Sixteenth ACM SIGSPATIAL International Conference on Advances in Geographic Information Systems*, Irvine, California